Photoacoustics 39 (2024) 100642

Contents lists available at ScienceDirect

Photoacoustics

journal homepage: www.elsevier.com/locate/pacs

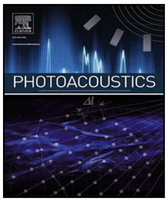

Research article

Numerical and in vitro experimental studies for assessing the blood hematocrit and oxygenation with the dual-wavelength photoacoustics

Subhadip Paul [a], Hari Shankar Patel [b], Vatsala Misra [c], Ravi Rani [c], Amaresh K. Sahoo [a], Ratan K. Saha [a,*]

[a] Department of Applied Sciences, Indian Institute of Information Technology Allahabad, Jhalwa, Prayagraj, 211015, U.P., India
[b] Laser Biomedical Applications Division, Raja Ramanna Centre for Advanced Technology, Indore, 452013, M.P., India
[c] Department of Pathology, Moti Lal Nehru Medical College, Prayagraj, 211002, U.P., India

ARTICLE INFO

Keywords:
Photoacoustics (PAs)
Radiative transport equation (RTE)
Oxygen saturation level (SO_2)
Total hemoglobin level (THB)
Hematocrit level (Hct)
Photoacoustic Monte-Carlo simulation (PAMC)

ABSTRACT

Assessing the blood hematocrit (Hct) and oxygenation (SO_2) levels are essential for diagnosing numerous blood-related diseases. This study examines the ability of the photoacoustic (PA) technique for quantitative evaluation of these parameters. We conducted the Monte Carlo and k-Wave simulations to compute PA signals at four different optical wavelengths from test blood samples followed by rigorous in vitro experiments. This method can estimate the Hct and SO_2 levels faithfully with ≥95% and ≥93% accuracies, respectively in the physiologically relevant hematocrits utilizing PA signals generated at 700 and 1000 nm optical wavelengths. A 2% decrease in the scattering anisotropy factor demotes SO_2 estimation by ≈ 27%. This study provides sufficient insight into how the opto-chemical parameters of blood impact PA emission and may help to develop a PA setup for in vitro characterization of human blood.

1. Introduction

Blood has been the subject of extensive research for long time. The whole blood is composed of various components, including red blood cells (RBCs), white blood cells, platelets, and plasma. In mammals, like humans, RBCs maintain a unique biconcave disk-shaped with a diameter ranging from 7.5 to 8.7 μm and a thickness of 1.7 to 2.2 μm [1–6]. They possess a flattened and depressed center, resembling a dumbbell-shaped cross-section, with a torus-shaped rim along the edges of the disk. The plasma serves as a suspending medium for the cells, with RBCs constituting nearly 99% of the cellular composition, averaging around 4–5 $\times 10^{12}$/L in a healthy adult [7]. Within the human body, blood plays a crucial role in the proper functioning of organs by facilitating the transport of nutrients and oxygen. Hemoglobin molecules, which make up RBCs, have a complex composition, consisting of carbon, hydrogen, nitrogen, oxygen, sulfur and iron. Hemoglobin demonstrates the remarkable ability to bind up to four oxygen molecules, forming oxyhemoglobin. While hemoglobin can also bind to carbon dioxide, this occurs to a lesser extent, resulting in the formation of carbaminohemoglobin [8]. As a result, the level of hemoglobin in the human body directly affects the amount of oxygen that can be transported. In a healthy adult, the typical hemoglobin level ranges from 140 to 180 g/L. Insufficient levels of hemoglobin lead to anemia, reducing the capacity for oxygen transport. According to the World Health Organization (WHO), approximately 19.3 million people, accounting for 27% of the global population, suffer from anemia [9]. Conversely, high hemoglobin count may occur due to chronic hypoxia and dehydration.

Accurate assessment of blood hemoglobin or hematocrit (Hct) and oxygen saturation (SO_2) levels are of profound clinical interest. Numerous techniques exist for measuring hemoglobin levels in vitro, including both qualitative methods [e.g., the copper sulfate technique (CST)] and quantitative approaches [such as the cyanmethemoglobin method (CM), hematology analyzer (AHA), the WHO Color Scale and point-of-care (POC) analyzers] [10]. To evaluate the SO_2 level, blood gas analyzers are routinely used in intensive care units and emergency departments [11,12]; resonance Raman Spectroscopy of Hb can also be conducted. These are noninvasive methods. Pulse oximeters that use near-infrared spectroscopy are globally accepted as noninvasive methods as well. Most notable among these is Masimo Pronto® Pulse CO-Oximeter which has found extensive clinical usages and can provide multiple blood parameters in vivo in real-time including total hemoglobin and blood oxygenation state [13,14].

A distinctive and potent method, photoacoustic (PA) spectroscopy, can simultaneously estimate the Hct and SO_2 levels by leveraging the

---

* Corresponding author.
E-mail addresses: rss2021008@iiita.ac.in (S. Paul), harish@rrcat.gov.in (H.S. Patel), drvatsalamisra@gmail.com (V. Misra), ranumishra22@rediffmail.com (R. Rani), asahoo@iiita.ac.in (A.K. Sahoo), ratank.saha@iiita.ac.in (R.K. Saha).

https://doi.org/10.1016/j.pacs.2024.100642
Received 23 June 2024; Received in revised form 1 August 2024; Accepted 27 August 2024
Available online 30 August 2024
2213-5979/© 2024 The Authors. Published by Elsevier GmbH. This is an open access article under the CC BY-NC license (http://creativecommons.org/licenses/by-nc/4.0/).

PA effect and spectroscopic principle [15]. The generation of acoustic waves due to absorption of light is known as the PA effect. The PA spectroscopy offers a non-invasive, highly sensitive and accurate means for estimating the blood Hct and SO_2 levels. The PA method is a potential candidate for in vivo assessment of these parameters. This technique relies on the distinctive optical absorption features of oxyhemoglobin (HbO) and deoxyhemoglobin (Hb). PA microscopy and tomography techniques exploit these aspects and can display spatial distributions of the Hct and SO_2 levels along with vascular structures. Therefore, images retaining anatomical and functional information can be formed using the PA schemes which may have clinical applications [16,17]. The PA technology has also been explored to develop POC devices [18,19].

Hochuli et al. extensively investigated the accuracy of the PA method for assessing the blood oxygen level and the role of selecting optimal wavelengths in their work [20]. Bench et al. employed a multiwavelength linear unmixing technique to estimate intravascular SO_2 levels [21]. Liu et al. developed an optical-resolution PA microscopy setup for simultaneous imaging of hemoglobin concentration, blood flow speed, and oxygen saturation with three-pulse excitation incorporating relaxation effect of the Grüneisen parameter [22]. Esenaliev et al. conducted fundamental studies on the applications of the PA technique in assessing the oxygenation levels in the internal jugular vein of sheep and humans [23–25]. Karpiouk et al. performed ultrasound and photoacoustic imaging of deep vein thrombosis for 532 nm exciting laser beam [26]. Hysi et al. observed changes in the PA spectral characteristics and blood oxygenation at different stages of RBC aggregation [27]. Saha et al. conducted PA studies on suspended and lyzed blood samples using wavelengths of 532 and 1064 nm [28]. Biswas et al. measured PA spectral response of blood clots of varying sizes [29]. Several other studies have also been performed for PA evaluation of blood pathologies [30–33]. These efforts have clearly established the potential of PA technology for the simultaneous determination of multiple blood parameters.

PA emission from a blood sample incredibly depends upon its optical properties, namely, absorption coefficient (μ_a), scattering coefficient (μ_s) and scattering anisotropy (g). These intrinsic parameters dictate the absorption and propagation of photons through the medium. A vast literature is available on the optical properties of blood. Some pioneering works are discussed herein. Faber et al. reported the scattering properties of oxygenated and deoxygenated whole blood from 250 to 1000 nm and also obtained the corresponding complex refractive indices utilizing a Kramers–Kronig analysis [34]. Meinke et al. examined the influence of platelets and plasma (PLS) on optical characteristics of blood [35]. The same properties of human blood were also measured in the spectral range of 250–2000 nm at Hct=33.2% by the same group. They deployed the Monte Carlo (MC) simulation to extract those parameters. In another study, the refractive index of human whole blood was measured in the visible and near-infrared ranges by Li et al. [36]. Bosschaart et al. incorporated formulas for the collective absorption coefficient and scattering coefficient of blood at different hematocrit levels [37]. They considered phosphate-buffered saline (PBS) as the suspending medium for RBCs. This modification aimed to provide a more realistic numerical representation of blood samples, enhancing the accuracy of optical studies. Some of the reports available in the literature also suggest that RBCs exposed to atmospheric conditions can directly absorb oxygen from the ambient environment [38,39].

The objective of the present work is to perform a comprehensive study on PA emission from blood. To achieve the same, both numerical and experimental means are employed. For the former approach, the MC simulations were carried out to determine the fluence maps in numerical blood phantoms. An exhaustive study was made on how to determine the optical properties of numerical blood samples depending on light absorption patterns at the molecular level and scattering features at the cellular level. The optical properties (μ_a, μ_s, and g) of the blood samples were calculated at 532, 700, 1000 and 1064 nm utilizing relevant formulas and published experimental data. No experiments have been conducted by us to determine the optical properties of the blood samples. To examine the impact of the surrounding medium, both PLS and PBS media were taken as the suspending fluids. The computed fluence maps were incorporated in the k-Wave toolbox generating the PA signals for those prototypes. PA experiments with in vitro blood samples were conducted in this study to experimentally validate our simulation results (RBCs suspended either in PBS or in PLS). Our numerical and experimental results demonstrate that the Hct level can be measured accurately with the PA technique. Our numerical study demonstrates that g parameter plays a vital role for the precise estimation of blood SO_2. Experimental study shows that the PA method can faithfully estimate the SO_2 level at the physiological hematocrit. The contributions of the current work are- (i) to present a rigorous study examining the dependence of hematocrit, oxygen saturation and surrounding medium on PA emission from blood using theoretical/numerical and experimental methods, (ii) to perform a comparative investigation to find out which optical wavelength pair can give optimal assessment of the blood parameters (Hct, SO_2) under different conditions, (iii) to demonstrate that the PA method cannot provide faithful estimation of the blood SO_2 when fluence maps vis-á-vis PA signals are simulated using g parameter evaluated via the Mie theory, which approximates RBCs as spheres, and (iv) to investigate the effect of the suspending medium (PBS/PLS) during the deoxygenation process of blood using N_2 purging.

The organization of the paper is as follows. Section 2 presents the theoretical models for light transport in tissue and propagation of PA waves in a fluid medium. The spectroscopic formulas for calculations of the blood Hct and SO_2 from PA signals are also included in Section 2. Numerical and experimental methods are detailed in Sections 3 and 4. The next section highlights the simulation and experimental results obtained from this study. Analysis of the results and important observations derived from this work are illustrated in Section 6. The conclusions of this study are summarized in this section as well.

2. Theoretical foundation

2.1. Photon transport in tissue

To understand the propagation of photons through a biological tissue, the diffusion equation (DE) is widely used. However, it is a special case (when $\mu_a \ll \mu_s$; medium almost reaches the scattering isotropy) of the most generalized radiative transfer equation (RTE). The RTE can explain the propagation of photons for both the ballistic and diffusion regimes. The RTE is given by [40],

$$\frac{1}{c}\frac{\partial \tilde{L}(\vec{r},\hat{\zeta},t)}{\partial t} = -\left(\hat{\zeta}.\nabla + (\mu_s+\mu_a)\right)\tilde{L}(\vec{r},\hat{\zeta},t) + \mu_s \int_{4\pi} \tilde{L}(\vec{r},\hat{\zeta}',t)\mathcal{U}(\hat{\zeta}'.\hat{\zeta})d\Omega' + \mathcal{S}(\vec{r},\hat{\zeta},t). \tag{1}$$

Eq. (1) is also known as the Boltzmann equation. Here, $\tilde{L}(\vec{r},\hat{\zeta},t)$ is the radiance; $\hat{\zeta}'$ and $\hat{\zeta}$ are the directions of incidence and scattering of a photon; c is the speed of light in vacuum; $\mathcal{U}(\hat{\zeta}'.\hat{\zeta})$ is the Henyey-Greenstein phase function, which is define as [41],

$$\mathcal{U}(\hat{\zeta}'.\hat{\zeta}) = \frac{1}{4\pi}\frac{(1-g^2)}{(1+g^2-2g\hat{\zeta}'.\hat{\zeta})} \tag{2}$$

where $\int_{4\pi}(\hat{\zeta}'.\hat{\zeta})\mathcal{U}(\hat{\zeta}'.\hat{\zeta})d\Omega = 1$ and $\hat{\zeta}'.\hat{\zeta} = \cos\theta$,

the incident beam and the scattered beam make an angle θ; Ω is the solid angle and $\mathcal{S}(\vec{r},\hat{\zeta},t)$ is the source term [40]. For a time invariant photon source,

$$\frac{1}{c}\frac{\partial \tilde{L}(\vec{r},\hat{\zeta},t)}{\partial t} = 0. \tag{3}$$

Therefore, Eq. (1) becomes,

$$\left[\hat{\zeta}.\nabla + (\mu_s+\mu_a)\right]L(\vec{r},\hat{\zeta}) = \mu_s\int_{4\pi} L(\vec{r},\hat{\zeta}')\mathcal{U}(\hat{\zeta}'.\hat{\zeta})d\Omega' + \mathcal{S}(\vec{r},\hat{\zeta}), \tag{4}$$

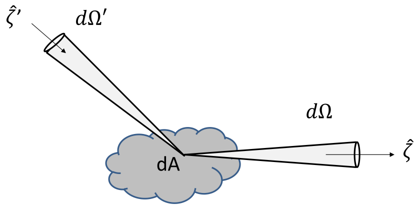

Fig. 1. Schematic of energy flow for a differential area element dA through the solid angle dΩ.

where $L(\vec{r}, \hat{\zeta})$ is the time-independent radiance. It is not straightforward to solve Eq. (4) analytically except for some simplistic geometry like an infinite slab or homogeneous medium possessing spherical/cylindrical symmetry. Being an integro-differential equation solving RTE is in general a very complex mathematical problem. No general analytical (closed-form) solutions of the RTE are available and it requires the use of advanced numerical methods, such as finite element method, integral transport methods, path integral method, and MC simulations, to solve RTE for nontrivial cases (see Fig. 1).

2.2. Photoacoustic wave equation

The time-dependent PA equation in 3D can be cast as,

$$\left(\vec{\nabla}^2 - \frac{1}{v^2}\frac{\partial^2}{\partial t^2}\right) p(\vec{r},t) = -\frac{\beta}{C_P}\frac{\partial \mathscr{H}(\vec{r},t)}{\partial t} \tag{5}$$

where β is the isobaric volume expansion coefficient in K^{-1}, C_P is the isobaric specific heat in J.K^{-1}, $\mathscr{H}(\vec{r},t)$ the heating function in W.m^{-3}, i.e., the amount of heat deposited per unit time per unit volume and $p(\vec{r},t)$ is the pressure at any arbitrary point at a location $\vec{r}$ at time t. The conditions of stress confinement and thermal confinement have been imposed while deriving Eq. (5). Let us consider time-varying laser beam incidents on the medium then,

$$\mathscr{H}(\vec{r},t) = I_0(\vec{r})\mu_a e^{-i\omega t}, \quad \text{with} \quad I_0(\vec{r},t) = \int_{4\pi} \tilde{L}(\vec{r},\hat{\zeta},t)\,d\Omega. \tag{6}$$

It may also be mentioned here that Eq. (5) for a Delta function heating pulse, $\mathscr{H}(\vec{r},t) = A(\vec{r})\delta(t)$, becomes,

$$\left(\vec{\nabla}^2 - \frac{1}{v^2}\frac{\partial^2}{\partial t^2}\right) p(\vec{r},t) = -\frac{p_0}{v^2}\frac{d\delta(t)}{dt}, \tag{7}$$

where $A(\vec{r})$ is the absorbance and the initial pressure rise is defined as, $p_0 = \Gamma \mu_a F$ with F as the fluence of the incident optical beam, which is given by,

$$F(\vec{r}) = \int_{-\infty}^{\infty} I_0(\vec{r},t)\,dt, \tag{8}$$

and $\Gamma = \frac{\beta v^2}{C_P}$ as the Grüneisen parameter. It is a dimensionless quantity and an important parameter for studying the thermal and elastic properties of matter. It is determined to be between 0.7 and 0.9, for fat tissue and 0.152 and 0.226 for blood [42].

2.3. Assessment of blood hematocrit and oxygen saturation

The peak-to-peak pressure (P_{pp}) can be determined as,

$$P_{pp} = max\left[p(\vec{r},t)\right] - min\left[p(\vec{r},t)\right]. \tag{9}$$

The total hemoglobin (THb) and blood oxygen saturation (SO$_2$) can be quantified as [43],

$$\text{THb} = C_{Oxy} + C_{deOxy} = \frac{P_{pp}^{\lambda_1}\Delta\epsilon^{\lambda_2} - P_{pp}^{\lambda_2}\Delta\epsilon^{\lambda_1}}{\epsilon_{deOxy}^{\lambda_1}\epsilon_{Oxy}^{\lambda_2} - \epsilon_{deOxy}^{\lambda_2}\epsilon_{Oxy}^{\lambda_1}} \tag{10}$$

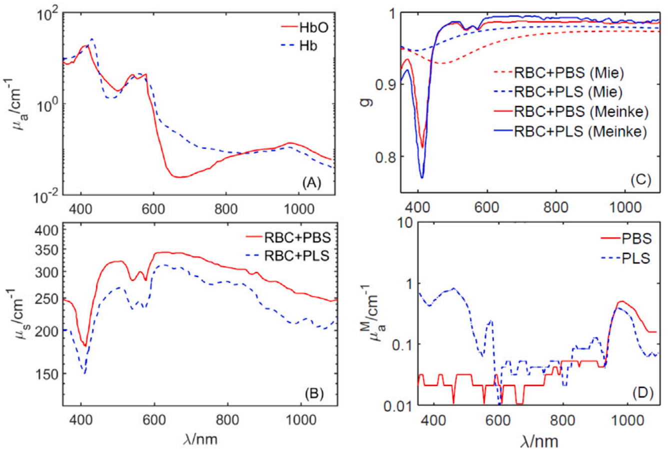

Fig. 2. (A) The optical absorption spectra for fully oxygenated and deoxygenated blood samples at Hct = 8% (data taken from Friebel et al. [45] and scaled properly to generate data for Hct = 8%). (B) The variation of optical scattering coefficient for different surrounding media at Hct = 8% (data taken from [35]). (C) Plots of scattering anisotropy factor calculated via the Mie theory assuming RBC as a homogeneous sphere (dash-dash lines); and the same plots (solid lines) are also generated using data taken from [35]. (D) The optical absorption spectra for PBS and PLS media (reproduced from [35]).

and

$$\text{SO}_2 = \frac{C_{Oxy}}{C_{Oxy} + C_{deOxy}} = \frac{P_{pp}^{\lambda_2}\epsilon_{deOxy}^{\lambda_1} - P_{pp}^{\lambda_1}\epsilon_{deOxy}^{\lambda_2}}{P_{pp}^{\lambda_1}\Delta\epsilon^{\lambda_2} - P_{pp}^{\lambda_2}\Delta\epsilon^{\lambda_1}} \tag{11}$$

respectively, λ_1 and λ_2 are the two incident optical wavelengths; C_{Oxy} and C_{deOxy} are the molar concentrations of oxy- and deoxy- hemoglobin molecules, respectively; ϵ_{Oxy} and ϵ_{deOxy} are the molar extinction coefficients of these molecules, respectively and $\Delta\epsilon^{\lambda} = \epsilon_{Oxy}^{\lambda} - \epsilon_{deOxy}^{\lambda}$. The molar extinction coefficients for HbO and Hb molecules can be found elsewhere [44]. Eqs. (10) and (11) have been derived from a spectroscopic formula by substituting the optical absorption coefficient with the corresponding PA amplitude [43]. It works well when the light energy density in the sample is constant. Eqs. (10) and (11) have been utilized in this study for assessing the total hemoglobin and oxygen saturation from numerical and experimental blood samples.

3. Numerical approaches

The optical properties of blood essentially depend upon various physical and chemical factors of the suspension. Many experimental investigations have been conducted to quantify μ_a, μ_s, and g for whole blood, as well as RBCs suspended in PBS, and plasma. The effect of the oxygenation state and lysis of the blood samples on optical properties have also been reported in the literature [35,37,41,45,46]. In this work, at first, μ_a, μ_s, and g of various blood samples were estimated. Accordingly, fluence distributions were obtained by performing the MC simulation. Finally, the computed fluence distributions were used as input to the k-Wave simulations for computing the PA signals from the samples under investigation. Blood parameters, namely, Hct and SO$_2$ were assessed from the simulated PA signals generated for two different optical wavelengths. The steps are described in the following sections.

3.1. Estimation of optical parameters of blood

3.1.1. Absorption coefficient

Let us consider $\mu_{a,Hct_0}^{Oxy/deOxy}$ as the measured light absorption coefficient at a wavelength for a fully oxygenated/deoxygenated blood sample with hematocrit Hct_0 (reference level) and we intend to estimate $\mu_{a,Hct}^{Oxy/deOxy}$ for the same type of blood sample but with hematocrit Hct and at the same wavelength. It can be readily calculated by demanding the extinction coefficient for the hemoglobin molecules

Table 1

The computed values of optical parameters (μ_a, μ_s and g) for a series of numerical blood samples under different hematocrit and oxygen saturation levels for various illuminating wavelengths (required for the MC simulations).

	Hct (%)	μ_a (cm^{-1})		μ_s (cm^{-1})		g (Mie calculation)		g (Meinke)		μ_a^M (cm^{-1})
		RBC+PLS [$SO_2 = 57\%$]	RBC+PBS [$SO_2 = 65\%$]	RBC+PLS	RBC+PBS	RBC+PLS	RBC+PBS	RBC+PLS	RBC+PBS	PLS/PBS
532 nm	50	211.79	215.45	445.04	542.56	0.969	0.939	0.979	0.976	0.11/0.02
	45	190.62	193.90	484.65	590.84	0.969	0.939	0.979	0.976	
	40	169.45	172.36	512.69	625.02	0.969	0.939	0.979	0.976	
	30	127.12	129.28	523.37	638.04	0.969	0.939	0.979	0.976	
700 nm	50	4.62	4.06	540.70	617.32	0.979	0.966	0.993	0.988	0.04/0.02
	45	4.16	3.66	588.82	672.26	0.979	0.966	0.993	0.988	
	40	3.71	3.25	622.89	711.15	0.979	0.966	0.993	0.988	
	30	2.79	2.44	635.87	725.97	0.979	0.966	0.993	0.988	
1000 nm	50	4.58	4.67	396.12	477.20	0.979	0.974	0.988	0.986	0.31/0.45
	45	4.15	4.25	431.37	519.68	0.979	0.974	0.988	0.986	
	40	3.72	3.83	456.33	549.74	0.979	0.974	0.988	0.986	
	30	2.87	2.98	465.84	561.19	0.979	0.974	0.988	0.986	
1064 nm	50	3.03	3.09	374.12	458.74	0.979	0.974	0.988	0.986	0.06/0.16
	45	2.74	2.80	407.42	499.57	0.979	0.974	0.988	0.986	
	40	2.44	2.51	430.99	528.47	0.979	0.974	0.988	0.986	
	30	1.84	1.92	439.97	539.48	0.979	0.974	0.988	0.986	

should be the same in both the samples. After some trivial steps, one obtains [37],

$$\begin{aligned}\mu_{a,Hct}^{Oxy/deOxy} = {} & \frac{Hct}{Hct_0}\left[\mu_{a,Hct_0}^{Oxy/deOxy} - Hct_0 f_{RBC}\mu_a^W\right] \\ & - \frac{Hct}{Hct_0}\left[(1-Hct_0)f_M\mu_a^M\right] + Hct f_{RBC}\mu_a^W \\ & + (1-Hct)f_M\mu_a^M,\end{aligned} \tag{12}$$

where the superscript W denotes water; the notation M indicates the surrounding medium (e.g., PBS or PLS); μ_a^W and μ_a^M are the light absorption coefficient for the water and the suspending medium, respectively; f_{RBC}, f_M are the fractional water contents in RBC and the surrounding medium, respectively; typical values are- $f_{RBC} = 0.66$, $f_M = 1$ for PBS and $f_M = 0.9$ for PLS [37]. Note that, in Eq. (12), light absorption by the water and the surrounding medium has been subtracted from that of the bulk medium.

Therefore, the absorption coefficient of a blood sample with arbitrary Hct and SO_2 levels can be estimated utilizing Eq. (12) and is given below,

$$\mu_{a,Hct} = \left[\eta\mu_{a,Hct}^{Oxy} + (1-\eta)\mu_{a,Hct}^{deOxy}\right], \tag{13}$$

where $\eta = SO_2$ is the oxygen saturation level of the blood sample.

The spectra for the optical absorption coefficient for fully oxygenated and deoxygenated blood samples at Hct_0=33.2% can be found in literature [45]. Similar curves at Hct=8% are generated by utilizing this dataset and employing Eq. (12). The curves are presented in Fig. 2(A). Moreover, the numerical value of μ_a for any blood sample with arbitrary Hct and SO_2 levels can thus be estimated from Eqs. (12) and (13). The corresponding value of μ_a^M has been taken from Fig. 2(D). Table 1 presents computed values of μ_a for a series of blood samples considered in this study.

3.1.2. Scattering coefficient

Let us now proceed to calculate the scattering coefficient of a blood sample ($\mu_{s,Hct}$) when that of a reference sample (μ_{s,Hct_0}) is known. The optical wavelength is constant. It may be emphasized here that the scattering cross-section of RBCs is a fundamental quantity (depends upon the size, shape of RBCs, and wavelength of the incident optical beam). It remains invariant though the Hct level may change [46]. Based on this argument, one can write [37],

$$\mu_{s,Hct} = \frac{(1-Hct)^2 Hct}{(1-Hct_0)^2 Hct_0}\mu_{s,Hct_0}. \tag{14}$$

where the term $(1-Hct)^2$ is a hematocrit-dependent scaling factor that relates dependent scattering (for the dense system) and independent scattering (for the sparse system). Various functional forms of the scaling factor have been chosen by various groups [47–49].

As in the previous case, many groups measured the optical scattering properties of RBCs under various experimental conditions. Fig. 2(B) demonstrates how μ_s changes with incident optical wavelength. Eq. (14) has been deployed to quantify μ_s for different blood samples considered in this study and are included in Table 1.

3.1.3. Scattering anisotropy factor

The anisotropy factor measures the amount of forward direction retained after a scattering event. For a spherical scatterer, g factor can be calculated by employing the Mie theory, which provides [50],

$$g = \frac{\int_0^\pi S_{11}\cos\theta\sin\theta d\theta}{\int_0^\pi S_{11}\sin\theta d\theta} \tag{15}$$

where, $S_{11} = \frac{1}{2}(S_1 + S_2)$; S_1 and S_2 are the scattering functions defined as [50,51],

$$S_1 = \sum_{n=1}^{\infty}\frac{2n+1}{n(n+1)}(q_n\pi_n + u_n\tau_n), \tag{16}$$

$$S_2 = \sum_{n=1}^{\infty}\frac{2n+1}{n(n+1)}(q_n\tau_n + u_n\pi_n), \tag{17}$$

respectively. The coefficients q_n and u_n dictate the amount of radiative transfer and are expressed as [52],

$$q_n = \frac{m^2 j_n(mx)[xj_n(x)]' - j_n(x)[mxj_n(mx)]'}{m^2 j_n(mx)[xh_n(x)]' - h_n(x)[mxj_n(mx)]'}, \tag{18}$$

$$u_n = \frac{j_n(mx)[xj_n(x)]' - j_n(x)[mxj_n(mx)]'}{j_n(mx)[xh_n(x)]' - h_n(x)[mxj_n(mx)]'}, \tag{19}$$

respectively. Here, $x = 2\pi a/\lambda$ with a as the radius of the scatterer and m is the refractive index of the scatterer with respect to the surrounding

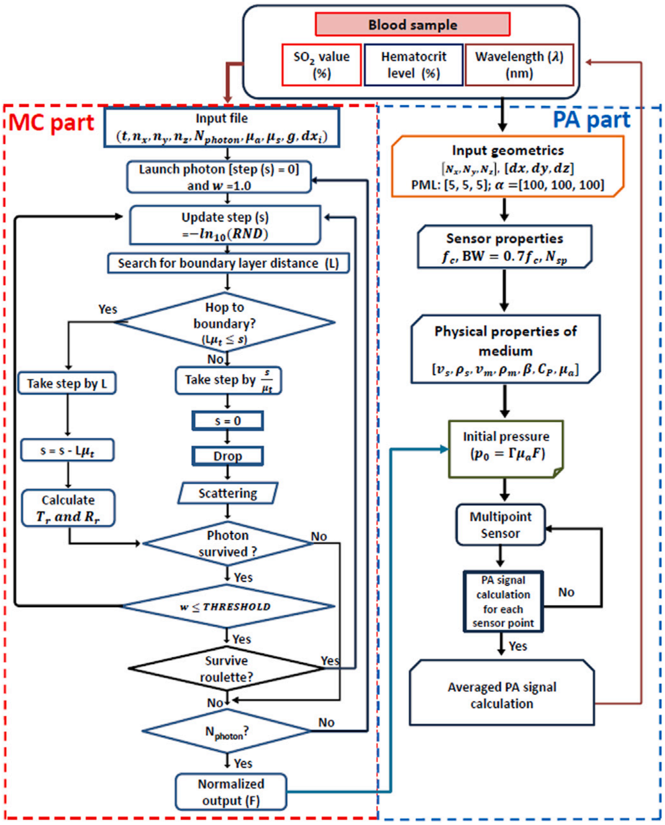
Blood sample
SO_2 value (%)
Hematocrit level (%)
Wavelength (λ) (nm)
MC part
Input file ($t, n_x, n_y, n_z, N_{photon}, \mu_a, \mu_s, g, dx_i$)
Launch photon [step (s) = 0] and w =1.0
Update step (s) $=-ln_{10}(RND)$
Search for boundary layer distance (L)
Hop to boundary? ($L\mu_t \leq s$)
Yes
No
Take step by L
Take step by $\frac{s}{\mu_t}$
$s = s - L\mu_t$
s = 0
Drop
Scattering
Calculate T_r and R_r
Photon survived ?
No
Yes
$w \leq THRESHOLD$
Yes
Survive roulette?
Yes
No
N_{photon}?
No
Yes
Normalized output (F)
PA part
Input geometrics
$[N_x, N_y, N_z]$, $[dx, dy, dz]$
PML: [5, 5, 5]; α =[100, 100, 100]
Sensor properties
f_c, BW $= 0.7f_c$, N_{sp}
Physical properties of medium
$[v_s, \rho_s, v_m, \rho_m, \beta, C_P, \mu_a]$
Initial pressure ($p_0 = \Gamma\mu_a F$)
Multipoint Sensor
PA signal calculation for each sensor point
No
Yes
Averaged PA signal calculation

Fig. 3. Flowcharts for the MC and k-Wave simulations.

medium; j_n and h_n are the spherical Bessel and Hankel functions of the first kind. The functions π_n and τ_n determine the angular scattering patterns. The corresponding formulas are,

$$\pi_n = \frac{2n-1}{(n-1)} \cos\theta \; \pi_{n-1} - \frac{n}{(n-1)} \pi_{n-2},$$
$$\tau_n = n\cos\theta \; \pi_n - (n+1)\pi_{n-1}, \tag{20}$$

with $\pi_0 = 0$ and $\pi_1 = 1$, respectively, In this work, an RBC has been approximated as a spherical object of radius $a = 2.75$ µm. Accordingly, the above set of equations have been numerically evaluated to predict the g values within the spectral bandwidth [see Fig. 2(C)] and are also inserted in Table 1. For comparison, g values extracted from the literature are presented in the same figure as well as in Table 1 [35].

3.2. Monte Carlo simulation

We use the MC multilayer (MCML) program for simulating photon propagation in homogeneous blood samples [53]. It has been proved to be a valuable numerical tool, which can provide insights into complex optical processes and help to analyze experimental data. The algorithm is summarized in Fig. 3 (left column). In this study, the size of the tissue volume was taken as, $(n_x, n_y, n_z) = (200, 200, 200)$. The individual voxels with edges $dx = dy = dz = 0.005$ cm span a total volume of 1.0 cm × 1.0 cm × 1.0 cm. The voxel size was arbitrarily chosen but the dimension of the simulation volume along the z-direction (the direction of propagation) corroborated with the sample holder (i.e., cuvette). The numerical values of the optical properties (μ_a, μ_s and g) of these voxels were taken from Table 1 depending upon the blood sample. However, ±1% fluctuation in μ_a value was introduced for some randomly chosen voxels (10% of the total voxel). This step was invoked to introduce noise in the simulated fluence map which might impact the performance of the PA technique for assessing the levels of Hct and SO_2.

The laser beam used in the simulation had a diameter (D_B) of 0.10 cm. The spatial profile of the beam along the lateral direction with respect to the direction of propagation was chosen to be uniform. The temporal profile of the beam was considered to be a delta function. For each simulation, 4 million photons were launched. The photons were only allowed to reflect back to the sample from the top surface (i.e. at $z = 0$). The photons were not permitted to reflect back to the sample from the side and bottom walls. The MC simulation provided fluence map for each sample. The simulations were executed in a server- Intel(R) Core(TM) Intel Core i7 12700 CPU, 2.1 GHz clock speed, 12 cores, 12 logical processors, Microsoft Windows 11 Professional OS, 128.0 GB DDR5 RAM, 16 GB NVIDIA RTX A4000 GPU with GCC-6.3.0-1 and MATLAB 2023b. A run time of 13 min was required for each MC simulation using 4 million photons.

3.3. k-Wave simulation

The k-Wave toolbox was used to perform the 3D acoustic simulations. The corresponding flowchart of the k-Wave simulation is displayed on the right column of Fig. 3. The 3D fluence matrix (F) for each sample (whose optical parameters are presented in Table 1) was obtained from the MC simulation as described above. The initial pressure rise, as defined earlier, for individual voxels was computed to be $p_0 = \Gamma\mu_a F$, Γ was taken to be unity for all samples. Banerjee et al. also simulated PA signals using fluence maps [54]. The size of the simulation domain was considered to be $(N_x, N_y, N_z) = (220, 220, 270)$ grid points and the grid size was fixed to $dx = dy = dz = 0.005$ cm. The thickness of the perfectly matched layer (PML) was chosen to be 0.05 cm. An anisotropic absorption coefficient of 100 np/m was introduced inside the PML to avoid reflections of ultrasound waves from the boundary walls. The widths of the k-Wave simulation domain along the x and y axes, excluding the PML layers, were the same as that of the MC simulation. The dimension of the k-Wave simulation domain along the z axis was chosen to be slightly longer than that of the MC simulation so that the transducer could be placed slightly away from the sample.

A circular aperture ultrasound transducer of radius 0.05 cm was placed at the coordinates $(N_x/2, N_y/2, N_z - 15)$. A total $N_{sp} = 317$ grid points essentially built the sensor. The center frequency and fractional bandwidth of the sensor points were set to be 2.25 MHz and 70%, respectively. The speed of sound and density of the sample and coupling medium were taken as, $v_s = v_m = 1500$ m/s and $\rho_s = \rho_m = 1000$ kg/m^3, respectively. The Courant–Friedrichs–Lewy number was set to 0.3 for the k-Wave simulations to reach numerical stability and as a result of that the sampling interval became 10 ns. The numerically evaluated time-dependent pressure data at the sensor points were stored. The Gaussian random noise was added with each simulated PA signal achieving the signal-to-noise ratio of 40 dB. The simulations were conducted for five different Hct levels, at two different SO_2 levels, and at four different optical wavelengths (532, 700, 1000, and 1064 nm). The PA signal generation at 532 and 1064 nm is of fundamental interest. The light absorption by Hb and HbO are significantly different as well as exhibit opposite trends at 700 and 1000 nm [see Fig. 2(A)]. That is why these two wavelengths were also considered. The simulations were performed in the same computer and the average execution time was about 22 s for each simulation (using graphics processing units).

3.4. Evaluation of the blood parameters

Eqs. (9), (10) and (11) were utilized in this study for PA estimations of the blood Hct and SO_2. The molar extinction coefficients for Hb and HbO were calculated from Fig. 2(A). The peak-to-peak amplitudes were calculated from the boundary signals only, where fluence distribution was uniform allowing us to use Eqs. (10) and (11). The computed peak-to-peak amplitudes for 700 and 1000 nm optical wavelengths for a series of Hct levels were inserted in Eq. (10) to calculate the THb for

Table 2

Details of the complete blood count (CBC) test for blood samples collected from three healthy volunteers; MCV, MCH and MCHC stand for mean corpuscular volume, mean corpuscular hemoglobin and mean corpuscular hemoglobin concentration, respectively.

Donor	Age	Sex	Hct (%)	THb (g/dL)	MCV (fL)	MCH (pg)	MCHC (g/dL)
1	27	M	39.2	13.8	85.7	30.3	35.4
2	30	M	44.6	15.3	83.4	28.6	34.3
3	33	F	41.0	14.3	73.9	25.7	34.8

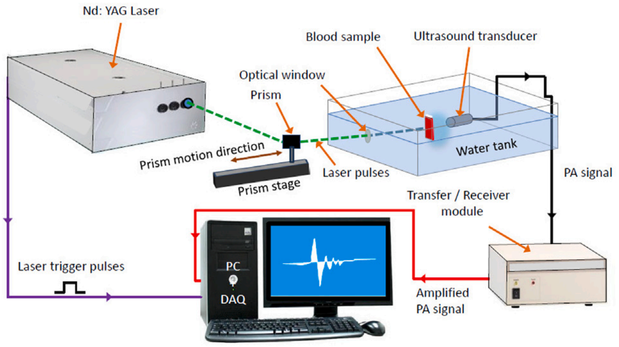

Fig. 4. A schematic of the experimental setup.

each sample. THb value obtained from the fitted line close to Hct=45% served as the calibration sample. It means that the calculated THb values, for a set of samples, were divided by that of the calibration sample and then multiplied by the Hct of the calibration sample. We termed it as the estimated Hct in the text. Moreover, the estimated Hct will exhibit minimum assessment error for the calibration sample. No such normalization was required while determining the SO_2 level because it is a dimensionless quantity see Eq. (11).

4. Experimental procedures

4.1. Sample preparation

Fresh venous blood of around 50 mL from a healthy human volunteer was collected with the permission of the ethical committee. The bag was prefilled with 7 ml of Citrate Phosphate Dextrose Adenine (CPDA) solution to prevent blood coagulation. Two types of blood samples were prepared as described herein. At first, the whole blood was centrifuged for 15 min at 3000 rpm. The plasma layer was gently removed and stored in a tube. The buffy coat was carefully discarded. The packed RBCs were gradually diluted with plasma and subsequently, the PA experiments were carried out. The Hct levels were varied approximately between 50 and 30%. This type of sample is referred to as RBC+PLS in the text and it was comparable to whole blood. Another set of samples was also prepared (indicated as RBC+PBS in the text). The whole blood was mixed with PBS and centrifuged for 15 min at 3000 rpm. The supernatant was eliminated and PBS was added. These steps were repeated three times to ensure proper washing of RBCs. Such packed RBCs were diluted with PBS sequentially to achieve different Hct levels in the same range and as mentioned earlier for each sample, PA data were recorded. The PA experiments with human blood were repeated for three times. Various blood parameters of the donors are inserted in Table 2.

4.2. PA signal detection

The schematic diagram of the setup used for the PA experiments is shown in Fig. 4. It included a tunable Nd:YAG laser system (EKSPLA, NT300 series) emitting pulses of 6 ns width and 10 Hz as the pulse repetition frequency (PRF). This instrument offers a range of wavelengths from 335 nm to 2500 nm (excluding the optical range 501–659 nm, but including 532 nm). A right-angle prism was employed to guide the beam so that it could fall on the blood sample. The blood sample was loaded into a glass cuvette (LARK, fluorescent optic glass cuvette). The cuvette filled with blood was placed in a water tank. The water medium acted as a coupling medium and its temperature remained constant at 23° C during the experiment. An unfocused ultrasound transducer (Panametric, V325-SU) with a center frequency of 2.25 MHz, 70% fractional bandwidth, and 1 cm diameter captured radio frequency (RF) signals. The detected PA signals were then amplified using a pulser/receiver module (JSR, DPR300). Finally, a data acquisition (DAQ) card (Adlink PCIe 9852) was employed to digitize the PA signals at a sampling frequency of 50 MHz and stored the RF lines each having 5000 data points. The trigger signal from the laser system was utilized to synchronize the DAQ system. For individual blood samples, 300 RF lines were recorded at each optical illumination for further analysis. The PA measurements were conducted at 532, 700, 1000 and 1064 nm optical wavelengths. The blood sample was softly but rigorously shaken between two consecutive PA experiments to avoid RBC precipitation.

The beam energy at 532, 700, 1000, and 1064 nm was measured to be 9.8, 12.5, 16.5 and 52.1 mJ/cm^2, respectively. Note that energy normalization was performed on the generated PA signal before computing the THb and SO_2 values by evaluating Eqs. (10) and (11), respectively. The exact Hct level was determined using a micro-centrifuge instrument. A capillary tube was loaded with blood; centrifuged for 2 min at 9000 rpm to ensure complete separation of RBCs and the suspending medium; then the Hct level was obtained using a Hct measurement scale. The SO_2 levels for experimental blood samples with the highest and lowest hematocrits with appropriate dilution were also evaluated using a UV–Vis instrument (PerkinElmer, Lambda 365+) for the same wavelength pairs. The absorption coefficients at 700 and 1000 nm were evaluated from the absorbance data (A), $\mu_a = 2.303A/l$, l being the pathlength. Thereafter the optical analog of Eq. (11) was employed to determine the blood SO_2. Finally, N_2 gas was purged through RBC+PLS and RBC+PBS samples for a sufficiently long time at a very low pressure to examine the role of the surrounding medium in gas absorption process by RBCs. The pH values were measured to be: RBC+PLS (before N_2 purging) = 6.61, RBC+PLS (after N_2 purging) = 6.52; RBC+PBS (before N_2 purging) = 6.90, RBC+PBS (after N_2 purging) = 6.72.

5. Simulation and experimental results

5.1. Outcomes of the simulation studies

Fig. 5 demonstrates the distributions of weights of photons (in log scale) inside some representative numerical blood samples having hematocrit levels, Hct=45% for all wavelengths considered in this study but for two SO_2 levels (SO_2 = 57% for RBC+PLS samples and SO_2 = 65% for RBC+PBS samples). A color bar is attached to quantify the color code in Fig. 5(d). The optical parameters for the MC simulations are taken from Fig. 2 and also summarized in Table 1. The columns 8 and 9 of Table 1 present the numerical values of g utilized in the simulations. The photons incident at z=0 and propagate along the z-direction. The photon beam penetrates very less into the sample at 532 nm compared to other wavelengths (compare Figs. 5(A) and (a) with others). The penetration is even more in cases of the PLS samples than those of the PBS counterparts. However, the beam spreads more in the lateral direction in the later samples in comparison to the former prototypes. It is obvious because the numerical value of g is marginally greater in a PLS medium than that of the corresponding PBS medium [compare

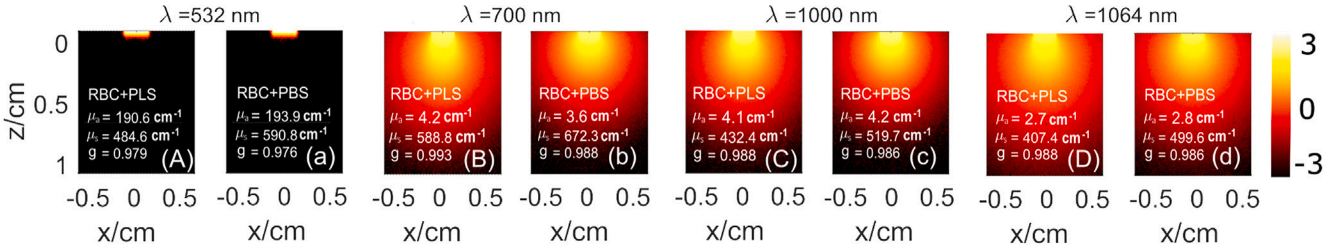

Fig. 5. Photon weight deposition map (in log scale) obtained from the MC simulation at 700 and 1000 nm wavelengths for RBC+PLS [(A)-(D)] and RBC+PBS [(a)-(d)] systems with Hct=45% and SO_2 = 57% and 65%, respectively; g values are taken from columns 8 and 9 of Table 1.

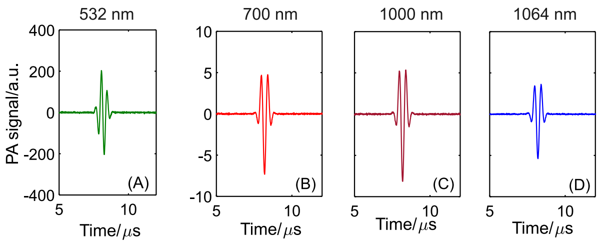

Fig. 6. Plots of the PA signals generated by the k-Wave toolbox utilizing the fluence maps produced by the MC simulation; RBC+PBS, Hct=45%, SO_2 = 65%.

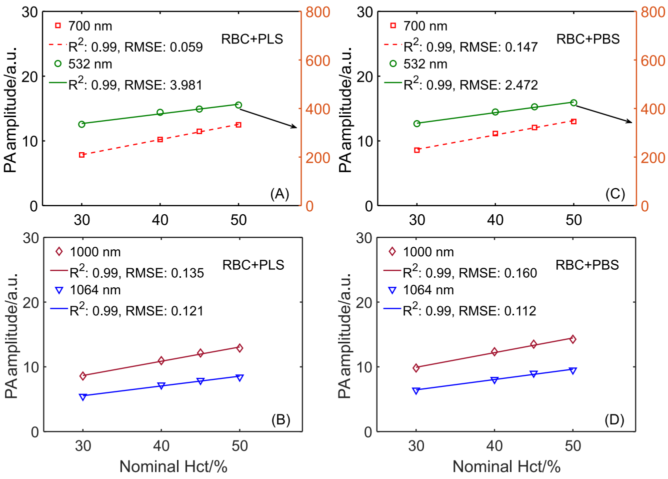

Fig. 7. (A)–(B) The graphs illustrate the variations of PA signal amplitude (peak-to-peak) with hematocrit level when RBCs with SO_2=57% are surrounded by the PLS medium. (C)–(D) Same as (A) and (B), respectively but for the PBS medium and SO_2=65%. R^2 provides goodness of a fitting and RMSE means root mean square error.

Figs. 5(B) and (b)]. The simulated PA signals generated by the k-Wave toolbox are displayed in Fig. 6. As expected blood sample emits a very strong PA signal at 532 nm than other optical wavelengths (compare Fig. 6(A) with others).

Representative plots of peak-to-peak PA signal amplitude as a function of hematocrit are shown in Fig. 7. As in the previous case g values have been taken from the literature (columns 8 and 9 of Table 1). The hematocrit level has been varied from 30 to 50% and incident optical wavelengths have been considered to be 532, 700, 1000, and 1064 nm. The plots of peak-to-peak amplitude are shown in the first column when RBCs are suspended in the PLS medium [Fig. 7(A) and (B)]. Similar graphs for the PBS medium are given in the second column [Fig. 7(C) and (D)]. The right y-axis acts as the scale for the 532 nm wavelength but for the other wavelengths the scale is placed on the left y-axis as usual. It can be seen from Fig. 7 that computed peak-to-peak amplitude exhibits monotonic rise with increasing hematocrit for all irradiating optical wavelengths. For each case, peak-to-peak data have been fitted with a straight line, which is also shown in each figure for convenience. The parameters, namely, goodness of fit (R^2) and root mean square error (RMSE) are also provided in the legend of each figure confirming excellent fit to the data points. It may be noted that similar plots (data not shown) can be generated if we use g values facilitated by the Mie theory (i.e., columns 6 and 7 of Table 1).

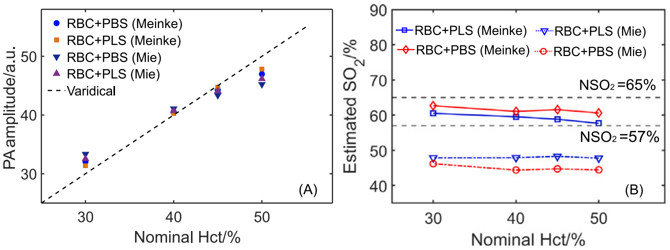

Fig. 8. (A) The nominal versus estimated Hcts. (B) The variation of evaluated SO_2 level with the ground truth Hct. The PA data have been simulated at 700 and 1000 nm optical wavelengths. The estimated SO_2 levels for various sources of g are illustrated for comparison [g values are calculated theoretically (Mie) in the first case but taken from the literature in the second case (Meinke)], NSO_2 means nominal SO_2.

After obtaining all the PA response lines at different wavelengths, the next task is to estimate the Hct and SO_2 levels for the blood samples using Eqs. (10) and (11). The PA data at a pair of optical wavelengths are required for assessing the Hct and SO_2 levels. The estimated values of blood Hct and SO_2, utilizing simulated data at 700 and 1000 nm wavelengths, are presented in Fig. 8. Note that both Mie and Meinke datasets have been implemented for generating the PA signals via the MC simulations. It is evident from Fig. 8(A) that the Hct levels can be predicated very accurately for both the PLS and PBS media (maximum error ≈ 7%). The Hct estimates for the Meinke dataset are marginally better than the Mie dataset at Hct=50%. Fig. 8(B) exhibits that the SO_2 levels are greatly underestimated for the Mie dataset. Average estimation errors are about −16% and −31% with respect to the ground truths for the RBC+PLS and RBC+PBS samples, respectively. Much improved assessments are possible when the forward simulations are conducted with the Meinke dataset. The SO_2 level can be accurately determined for the RBC+PLS samples whereas the average estimation error is about −**5.5**% with respect to the nominal value for the RBC+PBS systems. The simulation results for the Meinke dataset are also included in Table 3 (rows 3 to 6) for comparison with the experimental results. The quantitative results for other combinations of wavelengths are detailed in Tables S1 and S2.

5.2. Outcomes of the experimental studies

Some representative experimentally measured PA RF lines are displayed in Fig. 9. A thin but strong PA signal is generated at 532 nm. However, the PA signals are relatively thick for other incident optical wavelengths, this is because of deep penetrations of the light beams inside the samples. The plots of peak-to-peak amplitude with blood hematocrit are elaborated in Fig. 10 for four probing optical

Table 3
Assessed Hct and SO_2 levels from the generated PA signals at 700 and 1000 nm optical illuminations. Theoretical findings (rows 3 to 6) and experimental results for three donors (rows 7-10; rows 11-14 and rows 15-18, respectively) are presented for comparison. The SO_2 levels (columns 4 and 8, rows 7-18) for experimental blood samples with the highest and lowest hematocrits are obtained using a UV–Vis instrument for the same wavelength pairs.

	RBC+PLS				RBC+PBS			
	Nominal Hct (%)	**Estimated Hct (%)**	**Actual SO_2 (%)**	**Estimated SO_2 (%)**	**Nominal Hct (%)**	**Estimated Hct (%)**	**Actual SO_2 (%)**	**Estimated SO_2 (%)**
Meinke (Simulation)	50	47.8	57	57.6	50	46.9	65	60.6
	45	44.7	57	58.8	45	44.3	65	61.5
	40	40.3	57	59.5	40	40.5	65	61.0
	30	31.4	57	60.5	30	32.0	65	62.7
Donor 1 (Experiment)	49	48.5±1.4	59.0	54.3±1.9	50	48.8±1.4	61.4	70.4±3.3
	45	43.7±1.6	-	56.8±3.8	45	45.6±2.6	-	70.4±3.0
	40	39.0±2.4	-	61.5±3.5	35	37.0±1.7	-	70.2±3.7
	28	30.5±1.6	59.3	61.1±2.6	29	29.5±0.9	64.8	70.5±3.3
Donor 2 (Experiment)	49	46.6±1.6	59.7	52.5±2.7	50	53.6±0.7	62.1	59.1±1.1
	45	42.7±1.7	-	53.1±2.5	46	46.2±1.5	-	61.7±2.2
	39	44.2±0.9	-	50.2±1.9	42	39.9±0.8	-	61.4±1.5
	30	28.8±0.9	60.3	56.0±2.1	31	29.5±0.9	63.0	63.3±2.2
Donor 3 (Experiment)	50	51.2± 1.5	57.8	51.7±2.4	48	42.4± 0.6	59.4	58.9±1.6
	46	42.3± 1.4	-	55.8±2.4	44	40.5± 0.8	-	59.6±1.5
	40	39.1± 0.8	-	59.6±2.4	38	38.7± 1.2	-	57.7±2.5
	30	32.5± 1.4	59.1	51.8±3.0	30	34.0± 1.4	59.9	57.8±2.4

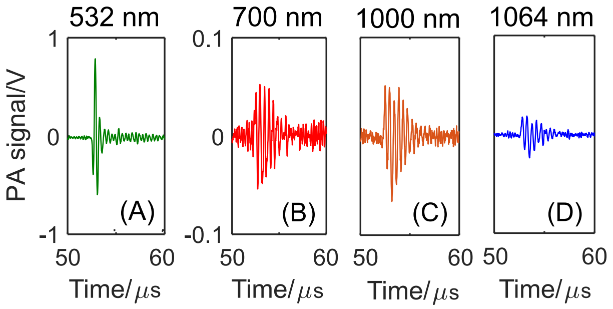

Fig. 9. (A)–(D) Representative PA signals experimentally measured at 532, 700, 1000 and 1064 nm incident optical wavelengths, respectively when RBCs are suspended in the PBS medium with $Hct = 45\%$ and $SO_2 \approx 70.4\%$.

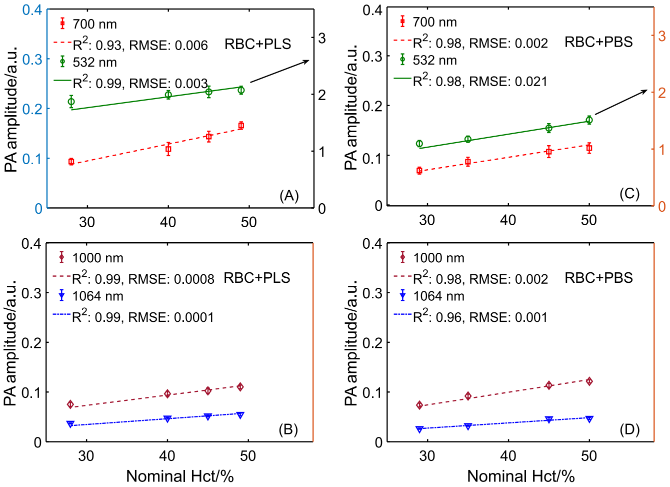

Fig. 10. Variation of peak-to-peak PA signal amplitude as a function of hematocrit; (A)–(B) cells are suspended in the PLS medium, (C)–(D) cells are dispersed in the PBS medium. The illuminating wavelengths are given in the legends. The computed values of R^2 and RMSE are also included in the legends.

wavelengths. This blood sample has been taken from donor1 whose blood parameters can be found in Table 2. A straightline fit to the experimental data is also presented for each case. It is clear from this figure that the linear fit works well for all cases which can be verified by examining the numerical values of fitness parameters (R^2 and RMSE). The peak-to-peak amplitude grows linearly with increasing hematocrit.

The PA estimation of blood Hct and SO_2 using experimental data for 700 and 1000 nm are shown in Fig. 11. The numerical values are further presented in Table 3 (rows 7 to 18). The PA method in general faithfully determines the blood Hct levels. It can be noted from Figs. 11(A), (C), (E) and Table 3 that average absolute errors in determining the blood Hct are ≈ 3%, 5.5% and 7% for donors 1, 2 and 3, respectively. The absolute error is calculated by including both classes of samples together (i.e., RBC+PLS, RBC+PBS) for each donor. Figs. 11(B), (D) and (F) denote how estimated SO_2 varies with Hct. Table 3 also displays the determined values of SO_2 (columns 5 and 9). For comparison, evaluated values of SO_2 using a UV–Vis instrument are inserted in the same table (columns 4 and 8). It is evident from these figures that the SO_2 levels for RBC+PLS and RBC+PBS samples are distinctly different for donors 1 and 2. The mean SO_2 levels are nearly 59% and 70%, respectively for donor 1. The same quantities are about 53% and 61%, respectively for donor 2. However, volunteer 3 exhibits greater variability with respect to volunteers 1 and 2 and such a trend is missing. The mean SO_2 levels can be calculated to be 54.7% and 58.5%, respectively. The estimated values of Hct and SO_2 for other

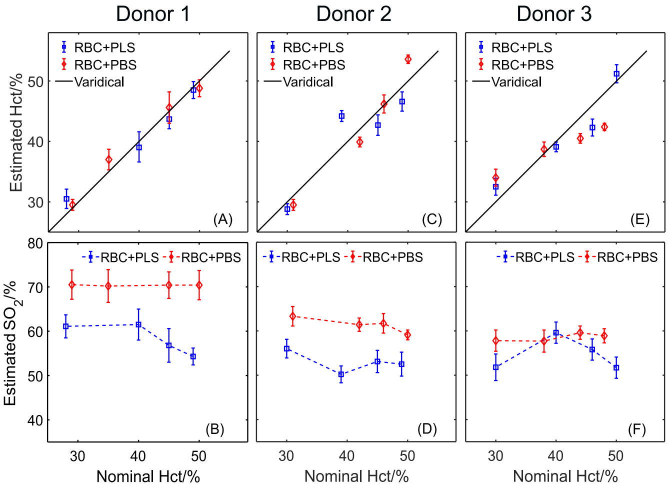

Fig. 11. PA determination of the blood Hct (top row) and SO_2 (bottom row) utilizing the PA signals measured at 700 and 1000 nm optical wavelengths.

combinations of optical wavelengths are highlighted in Tables S3, S4, and S5, respectively.

6. Discussion and conclusions

In this work, PA emission from blood has been investigated at different optical wavelengths. The role of the surrounding medium (PLS/PBS) on PA emission is also examined. At first, numerical studies are performed rigorously. The optical parameters (μ_a, μ_s and g) for a series of blood samples have been theoretically estimated. These parameters are utilized to run the MC simulations providing fluence maps for those samples which are subsequently used to execute the k-Wave simulations to compute the PA signals. MC noise and Gaussian noise have been added while executing these simulations, respectively. The peak-to-peak amplitudes of simulated PA signals at 700 and 1000 nm are employed to assess the blood Hct and SO_2 levels. The peak-to-peak amplitude demonstrates linear increase with increasing Hct (see Figs. 6 and 10). This is in contrast to nonlinear growth of PA signals observed by other groups in various contexts [54,55].

The Hct can be estimated with good accuracy with the PA method which can be confirmed from rows 3 to 6 of Table 3. For instance, for the numerical study, the average absolute error in estimating Hct is about 4% (with 40 dB noise). The same errors can be found to be approximately 3 and 8% when the noise levels are 20 and 10 dB, respectively (data not shown for 20 and 10 dB noise levels). Similarly, the average absolute errors in determining SO_2 can be calculated to be 5, 4 and 7% for 40, 20 and 10 dB noise levels, respectively. It is also true for experimental studies (absolute errors are within 7% for Hct estimations). The predicted SO_2 levels by the PA technique are in general consistent with the actual values obtained from the UV–Vis method (compare columns 4 and 5; 8 and 9 of the same table). For donor 1 and for RBC+PBS samples, the PA estimations are slightly on the higher side compared to the nominal values of SO_2 (see columns 8 and 9, rows 7–10 of Table 3). It may also be mentioned here that SO_2 level in some cases marginally decreases with increasing hematrocit (see Fig. 11), which is consistent with the simulated trend (see Fig. 8). However, the opposite trend was reported by [27]. Further investigations are required to understand the reasons behind such observations.

One of the reasons for incorrect estimation of blood SO_2 may be that optical absorption by the ambient medium is not considered by Eq. (11). The peak-to-peak amplitude line should pass through the origin in the absence of the background absorption and consequently, the PA technique may offer accurate SO_2 prediction. Nevertheless, background absorption may not be negligible at certain optical wavelengths. Fig. 12(A) exhibits how PA amplitude varies with wavelength for PLS/PBS medium. Accordingly, the y-intercept of the peak-to-peak amplitude line may become nonzero in case of finite background absorption which may result in erroneous SO_2 evaluation. This aspect was investigated elaborately in this study but no significant improvement was made. For PA experiments, there exists a possibility of temperature rise of the sample because of absorption of light energy and thus signal amplitude may grow leading to increased estimations of the blood Hct and SO_2. Recently, Grüneisen relaxation effect is compensated for in the oxygen saturation calculation [22]. A similar strategy may also be adopted for the determination of blood SO_2.

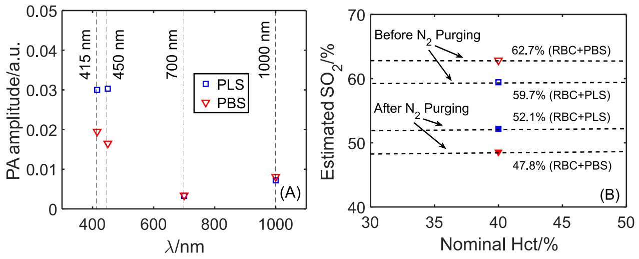

Fig. 12. (A) The measured PA amplitudes for the PBS and PLS fluids. (B) The graph illustrates the change in oxygen level before and after N_2 purging for RBC+PLS and RBC+PBS samples with $Hct = 40\%$.

Note that g values facilitated by the Mie theory approximating RBCs as homogeneous spheres appear to be on the lower side (see Table 1). It also considers constant refractive indices for RBC and the ambient medium ($n_{RBC} = 1.47$, $n_{PLS} = 1.35$ and $n_{PBS} = 1.33$ at 600 nm) [35]. On the other hand, g values extracted from experimental data are found to be on the higher side [35]. It may be mentioned here that accurate experimental determination of g parameter requires a very dilute sample with Hct ≈ 1% or less [35]. Fig. 8(B) clearly shows that the estimation of SO_2 deviates greatly when forward simulations are conducted with the g values provided by the Mie theory. Whereas, significantly improved estimation is possible when g values provided by the Meinke dataset are used. The incident photons scatter more in the lateral direction when the g value is small. Hence, the PA source will become thin but wide, the corresponding PA pulse will be narrow but strong. On the other hand, when the g value is large, the forward direction is preferred after scattering and the PA source will shrink in the lateral direction but elongate in the forward direction. The width of the associated PA pulse will become broad with reduced amplitude (compared to the previous case). These small alterations contribute favorably leading to improved estimation of blood SO_2. In other words, a small variation of g factor can induce a large error in SO_2 assessment. This is one of the important findings of this work. This observation may be useful while investigating pathological blood samples with PAs. Note that there exist many pathological conditions (e.g., autoimmune diseases and malaria infection; aggregation and lysis of RBCs), which can modify the g factor and may impact the PA estimations of blood Hct and SO_2.

As mentioned above, it is found that the SO_2 levels for the RBC+PBS samples are in general measured to be slightly higher than that of the RBC+PLS samples. It may be argued that various macromolecules present in the PLS medium form a layer on the surface of RBCs and that inhibit gas diffusion process. However, such a layer is removed during rigorous washing of RBCs promoting the possibility of gas exchange between the cell and the suspending fluid. To further confirm this aspect, N_2 gas was purged into two samples (RBC+PLS and RBC+PBS) for sufficiently long time. It has been observed that SO_2 level drops about 8% for the first sample whereas it is about 15% for the second sample. The results are shown in Fig. 12(B). Therefore, it is highly likely that during blood processing, RBCs absorbed oxygen dissolved in the saline water and from the atmosphere elevating the SO_2 level [38,39].

In conclusion, this work reports a comprehensive study on PA response of human blood involving rigorous numerical and in vitro experimental investigations. Theoretical formulas exploiting the fundamental principles of physics are described for calculations of the optical parameters of blood. It is found that the PA technique can assess blood Hct with high accuracy ($\geq 95\%$). The mean accuracy for estimating the level of blood SO_2 has been determined to be $\geq 93\%$. The simulation study demonstrates that a small change (2% decrement) in g value of the sample can lead to a large change ($\approx$ 27% drop) in the SO_2 estimation. The Mie theory approximates RBCs as homogeneous spheres and the g estimates are calculated to be slightly less than that of the Meinke dataset, which incorporates the actual size and shape of RBCs. In other words, this study proves that a minor morphological change in the microscopic level (which is much smaller than the acoustic detection wavelength corresponding to 2.25 MHz) has of profound impact in the assessment of bulk SO_2. Further experimental works are required to carefully analyze how PA signal is affected by changes in the optical parameters (i.e., for pathological blood samples). More specifically, this theoretical approach accounting for cellular morphology needs to be employed for PA signal simulation and validated experimentally for realizing the goal of developing a portable PA system for simultaneous measurement of multiple blood parameters.

CRediT authorship contribution statement

Subhadip Paul: Writing – review & editing, Writing – original draft, Methodology, Investigation, Formal analysis, Data curation, Conceptualization. **Hari Shankar Patel:** Writing – review & editing, Writing – original draft, Supervision, Methodology, Conceptualization. **Vatsala Misra:** Writing – review & editing, Writing – original draft, Supervision, Resources, Methodology, Funding acquisition, Conceptualization. **Ravi Rani:** Writing – review & editing, Writing – original draft, Resources, Methodology, Funding acquisition. **Amaresh K. Sahoo:** Writing – review & editing, Writing – original draft, Supervision, Methodology, Investigation, Funding acquisition, Conceptualization. **Ratan K. Saha:** Writing – review & editing, Writing – original draft, Supervision, Methodology, Investigation, Funding acquisition, Formal analysis, Conceptualization.

Declaration of competing interest

The authors declare that there are no competing interests.

Data availability

Data will be made available on request.

Acknowledgments

We are thankful to Mr. Vinod Tiwari and Mr. Anil Tiwari, Blood Bank, Swaroop Rani Nehru Hospital for providing blood samples; Mr. Vinod Pathak, Health Center, IIIT Allahabad for his assistance during pathological work. We also appreciate continuous support received from the members of the Biomedical Imaging Laboratory (BMIL) at IIIT Allahabad. HSP acknowledges the support received from Dr. S. K. Majumder, Head, Laser Biomedical Applications Division, Raja Ramanna Centre for Advanced Technology, Indore (MP) India. The work is supported by the Indian Council of Medical Research (56/2/2020-Hae/BMS).

Appendix A. Supplementary data

Supplementary material related to this article can be found online at https://doi.org/10.1016/j.pacs.2024.100642.

References

[1] M. Diez-Silva, M. Dao, J. Han, C.T. Lim, S. Suresh, Shape and Biomechanical Characteristics of Human Red Blood Cells in Health and Disease, MRS Bull. 35 (5) (2010) 382–388, http://dx.doi.org/10.1557/mrs2010.571.

[2] R.K. Saha, Computational modeling of photoacoustic signals from mixtures of melanoma and red blood cells, J. Acoust. Soc. Am. 136 (4) (2014) 2039–2049.

[3] B.J. Bain, Haematology Case Studies with Blood Cell Morphology and Pathophysiology I, Singh, A. Weston & A. Kundur Academic Press, London, 2017.

[4] G. Rozenberg, Microscopic Haematology: A Practical Guide for the Laboratory, Elsevier Australia, 2011.

[5] H.K. Walker, W.D. Hall, J.W. Hurst, Clinical Methods: The History, Physical, and Laboratory Examinations, Butterworths, 1990.

[6] R. Oishi, M. Hasegawa, T. Hakozaki, S. Obara, T. Isosu, M. Murakawa, The accuracy of noninvasive total hemoglobin measurement in critically ill patients, Rev. Bras. Anestesiol. 69 (2019) 527–528.

[7] W.O. Reece, E.W. Rowe, Functional Anatomy and Physiology of Domestic Animals, John Wiley & Sons, 2017.

[8] D. Treacher, R. Leach, Oxygen transport—1. Basic principles, BMJ 317 (7168) (1998) 1302–1306.

[9] R.D. Whitehead Jr., Z. Mei, C. Mapango, M.E.D. Jefferds, Methods and analyzers for hemoglobin measurement in clinical laboratories and field settings, Ann. New York Acad. Sci. 1450 (1) (2019) 147–171.

[10] A. Singh, A. Dubey, A. Sonker, R. Chaudhary, Evaluation of various methods of point-of-care testing of haemoglobin concentration in blood donors, Blood Transfus. 13 (2) (2015) 233.

[11] N. Korpi-Steiner, G. Horowitz, M. Tesfazghi, B.B. Suh-Lailam, Current issues in blood gas analysis, J. Appl. Lab. Med. 8 (2) (2023) 372–381.

[12] I. Torres Filho, N.M. Nguyen, R. Jivani, J. Terner, P. Romfh, D. Vakhshoori, K.R. Ward, Oxygen saturation monitoring using resonance Raman spectroscopy, J. Surg. Res. 201 (2) (2016) 425–431.

[13] P. Panda, M. Sen, Accuracy of haemoglobin estimation by non-invasive pulse co-oximetry method: A prospective observational study among neonates, children and Young adults, J. Med. Res. 4 (1) (2018) 10–15.

[14] M.F. Young, K. Raines, F. Jameel, M. Sidi, S. Oliveira-Streiff, P. Nwajei, K. McGlamry, J. Ou, A. Oladele, P.S. Suchdev, Non-invasive hemoglobin measurement devices require refinement to match diagnostic performance with their high level of usability and acceptability, PLoS One 16 (7) (2021) e0254629.

[15] A. Hussain, W. Petersen, J. Staley, E. Hondebrink, W. Steenbergen, Quantitative blood oxygen saturation imaging using combined photoacoustics and acousto-optics, Opt. Lett. 41 (8) (2016) 1720–1723.

[16] I. Steinberg, D.M. Huland, O. Vermesh, H.E. Frostig, W.S. Tummers, S.S. Gambhir, Photoacoustic clinical imaging, Photoacoustics 14 (2019) 77–98.

[17] L. Lin, L.V. Wang, The emerging role of photoacoustic imaging in clinical oncology, Nature Rev. Clin. Oncol. 19 (6) (2022) 365–384.

[18] M.K.A. Singh, N. Sato, F. Ichihashi, Y. Sankai, LED-based photoacoustic imaging: a point-of-care solution for microvascular health assessment, in: Photons Plus Ultrasound: Imaging and Sensing 2024, vol. 12842, SPIE, 2024, pp. 193–199.

[19] M.K.A. Singh, N. Sato, F. Ichihashi, Y. Sankai, Point-of-care functional and molecular imaging using LED-based photoacoustics, in: TENCON 2019-2019 IEEE Region 10 Conference, TENCON, IEEE, 2019, pp. 109–113.

[20] R. Hochuli, L. An, P.C. Beard, B.T. Cox, Estimating blood oxygenation from photoacoustic images: can a simple linear spectroscopic inversion ever work? J. Biomed. Opt. 24 (12) (2019) 121914.

[21] C. Bench, B. Cox, Quantitative photoacoustic estimates of intervascular blood oxygenation differences using linear unmixing, in: Journal of Physics: Conference Series, vol. 1761, no. 1, IOP Publishing, 2021, 012001.

[22] C. Liu, Y. Liang, L. Wang, Single-shot photoacoustic microscopy of hemoglobin concentration, oxygen saturation, and blood flow in sub-microseconds, Photoacoustics 17 (2020) 100156.

[23] R.O. Esenaliev, I.V. Larina, K.V. Larin, D.J. Deyo, M. Motamedi, D.S. Prough, Optoacoustic technique for noninvasive monitoring of blood oxygenation: a feasibility study, Appl. Opt. 41 (22) (2002) 4722–4731.

[24] Y.Y. Petrov, I.Y. Petrova, I.A. Patrikeev, R.O. Esenaliev, D.S. Prough, Multiwavelength optoacoustic system for noninvasive monitoring of cerebral venous oxygenation: a pilot clinical test in the internal jugular vein, Opt. Lett. 31 (12) (2006) 1827–1829.

[25] I.Y. Petrov, D.S. Prough, Y. Petrov, S.N. Henkel, R. Seeton, R.O. Esenaliev, Simultaneous measurements of total hemoglobin concentration and blood oxygenation with laser diode-based optoacoustic system, in: Photons Plus Ultrasound: Imaging and Sensing 2017, vol. 10064, SPIE, 2017, pp. 111–116.

[26] A.B. Karpiouk, S.R. Aglyamov, S. Mallidi, J. Shah, W.G. Scott, J.M. Rubin, S.Y. Emelianov, Combined ultrasound and photoacoustic imaging to detect and stage deep vein thrombosis: phantom and ex vivo studies, J. Biomed. Opt. 13 (5) (2008) 054061.

[27] E. Hysi, R.K. Saha, M.C. Kolios, Photoacoustic ultrasound spectroscopy for assessing red blood cell aggregation and oxygenation, J. Biomed. Opt. 17 (12) (2012) 125006.

[28] R.K. Saha, S. Karmakar, M. Roy, Photoacoustic response of suspended and hemolyzed red blood cells, Appl. Phys. Lett. 103 (4) (2013).

[29] D. Biswas, S. Vasudevan, G.C. Chen, N. Sharma, Quantitative photoacoustic characterization of blood clot in blood: A mechanobiological assessment through spectral information, Rev. Sci. Instrum. 88 (2) (2017) 024301.

[30] J. Brunker, P. Beard, Erratum: Acoustic resolution photoacoustic Doppler velocimetry in blood-mimicking fluids, Sci. Rep. 6 (2016).

[31] S. Banerjee, S. Sarkar, S. Saha, S.K. Hira, S. Karmakar, Observing temporal variation in hemolysis through photoacoustics with a low cost LASER diode based system, Sci. Rep. 13 (1) (2023) 7002.

[32] F.J. Bodera, M.J. McVey, K. Sathiyamoorthy, M.C. Kolios, Detection of clot formation & lysis In-Vitro using high frequency photoacoustic imaging & frequency analysis, Photoacoustics 30 (2023) 100487.

[33] P.P. Pai, P.K. Sanki, S. Banerjee, A photoacoustics based continuous non-invasive blood glucose monitoring system, in: 2015 IEEE International Symposium on Medical Measurements and Applications (MeMeA) Proceedings, IEEE, 2015, pp. 106–111.

[34] D.J. Faber, M.C. Aalders, E.G. Mik, B.A. Hooper, M.J. van Gemert, T.G. van Leeuwen, Oxygen saturation-dependent absorption and scattering of blood, Phys. Rev. Lett. 93 (2) (2004) 028102.

[35] M. Meinke, G. Müller, J. Helfmann, M. Friebel, Optical properties of platelets and blood plasma and their influence on the optical behavior of whole blood in the visible to near infrared wavelength range, J. Biomed. Opt. 12 (1) (2007) 014024.

[36] H. Li, L. Lin, S. Xie, Refractive index of human whole blood with different types in the visible and near-infrared ranges, in: Laser-Tissue Interaction XI: Photochemical, Photothermal, and Photomechanical, vol. 3914, SPIE, 2000, pp. 517–521.

[37] N. Bosschaart, G.J. Edelman, M.C. Aalders, T.G. van Leeuwen, D.J. Faber, A literature review and novel theoretical approach on the optical properties of whole blood, Lasers Med. Sci. 29 (2014) 453–479.

[38] S. Tuvia, S. Levin, R. Korenstein, Oxygenation-deoxygenation cycle of erythrocytes modulates submicron cell membrane fluctuations, Biophys. J. 63 (2) (1992) 599–602.

[39] D. Castro, S.M. Patil, M. Zubair, M. Keenaghan, URL: https://www.ncbi.nlm.nih.gov/books/NBK536919/. (Accessed 20 September 2023).

[40] L.V. Wang, H.-i. Wu, Biomedical Optics: Principles and Imaging, John Wiley & Sons, 2012.

[41] S.L. Jacques, Optical properties of biological tissues: a review, Phys. Med. Biol. 58 (11) (2013) R37.

[42] D.-K. Yao, C. Zhang, K. Maslov, L.V. Wang, Photoacoustic measurement of the Grüneisen parameter of tissue, J. Biomed. Opt. 19 (1) (2014) 017007.

[43] X. Wang, X. Xie, G. Ku, L.V. Wang, G. Stoica, Noninvasive imaging of hemoglobin concentration and oxygenation in the rat brain using high-resolution photoacoustic tomography, J. Biomed. Opt. 11 (2) (2006) 024015.

[44] S. Prahl, Optical absorption of hemoglobin, 1999, http://omlc.ogi.edu/spectra/hemoglobin.

[45] M. Friebel, J. Helfmann, U. Netz, M. Meinke, Influence of oxygen saturation on the optical scattering properties of human red blood cells in the spectral range 250 to 2000 nm, J. Biomed. Opt. 14 (3) (2009) 034001.

[46] M. Fribel, Determination of optical properties of human blood in the spectral range 250 to 1100 nm using Monte Carlo simulations with hematocrit-dependent effective scattering phase functions, J. Biomed. Opt. 11 (3) (2006) 34921.

[47] J.M. Steinke, A. Shepherd, Comparison of Mie theory and the light scattering of red blood cells, Appl. Opt. 27 (19) (1988) 4027–4033.

[48] J.K. Percus, G.J. Yevick, Analysis of classical statistical mechanics by means of collective coordinates, Phys. Rev. 110 (1) (1958) 1.

[49] V. Twersky, Acoustic bulk parameters in distributions of pair-correlated scatterers, J. Acoust. Soc. Am. 64 (6) (1978) 1710–1719.

[50] C.F. Bohren, D.R. Huffman, Absorption and Scattering of Light by Small Particles, John Wiley & Sons, 2008.

[51] C. Mätzler, MATLAB Functions for Mie Scattering and Absorption, Version 2, Institute of Applied Physics, University of Bern, 2002.

[52] M. Hartmann, Light Scattering by Small Particles. By HC van de Hulst, New York (John Wiley and Sons), London (Chapman and Hall), 1957.

[53] L. Wang, S.L. Jacques, L. Zheng, MCML— Monte Carlo modeling of light transport in multi-layered tissues, Comput. Methods Programs Biomed. 47 (2) (1995) 131–146.

[54] S. Banerjee, S. Sarkar, S. Karmakar, Acquiring photoacoustic signature of hematocrit variation from plexus layer of in-silico human skin phantom, Biomed. Phys. Eng. Express 7 (3) (2021) 035007.

[55] R. Gao, Z. Xu, Y. Ren, L. Song, C. Liu, Nonlinear mechanisms in photoacoustics–powerful tools in photoacoustic imaging, Photoacoustics 22 (2021) 100243.

Mr. Subhadip Paul is a Ph.D. scholar of the Department of Applied Sciences, IIIT Allahabad. He has joined the Biomedical Imaging group in 2021. He obtained his master of science degree (major in physics) from the Indian Association for Cultivation of Science, Kolkata, India. Currently he is involved in conducting various experimental studies with photoacoustic.

Dr. Hari Shankar Patel is currently working as a Scientific Officer G at the Raja Ramanna Centre for Advanced Technology (RRCAT), Indore, India. His research interest lies in the field of biomedical optics and applications of laser technology in biomedical problems. He has conducted many simulation and experimental studies in biomedical optics.

Prof. Vatsala Misra is the Head of the Department of Pathology at Moti Lal Nehru Medical College, Allahabad, U.P. She is member of many national and international societies. She is actively involved in research and academic work and has published more than 185 papers in national and international journals. She is on the editorial advisory board and reviewer panel of many national and international journals and she worked as the Editor-in Chief of Indian Journal of Pathology and Microbiology from 2013-2017. Her main field of research is Gastrointestinal pathology and cytology. She is one of the first authors to work on portal hypertensive vasculopathy (gastropathy, colopathy and enteropathy) from India. She has done a lot of work on *H. pylori* and recently working on role of HPV in Upper G. I. Tract lesions and oral lesions. She has keen interest in Hematology and transfusion medicines also. She is also incharge of bloodbank of the hospital.

Ravi Rani She has done her MD in pathology. Her area of interest is transfusion medicine and hematology. At Moti Lal Neheru Medical College, she leads a team of 24 staffs. She supervises the work of blood donation, blood component preparation, blood storage, document maintenance and overall quality control of transfusion medicine. She regularly conducts blood donation camps. At the clinical pathology laboratory, several tests like liver function test, kidney function test, hormonal profile, CBC are carried out regularly. Daily workload of the clinical pathology laboratory is around 300 samples (blood and urine) per day. Her association with the proposed project will be very much beneficial.

Dr. Amaresh Kumar Sahoo has been serving as an Assistant Professor of the Department of Applied Sciences, IIIT Allahabad since 2016. He has done Ph.D. in Nanobiotechnology and subsequent post-doctoral research in the area of Nano-biosensors. His research works mainly focused on the 'theranostic' applications of the novel nanoscale materials. He also, carried out substantial amount of works in antibacterial study, drug/gene delivery to the cancer cells and bio-imaging. During his Ph.D. and post-doc he has garnered experience in synthesis, characterization and biological applications of the various types of nanoscale materials. He has expertise in flow cytometry (FACS) and confocal microscopy imaging, PCR etc. He has expertise in both cell culture as well as bacterial culture.

Dr. Ratan Kumar Saha is currently an Associate Professor of the Department of Applied Sciences, IIIT Allahabad. He studied ultrasound scattering from single cell and many cells (e.g. nonaggregated and aggregated RBCs, normal and apoptotic cancer cells etc.). He also developed an experimental set up for measuring angular distribution of ultrasound scattering. In case of photoacoustics, the primary focus is to understand, using theoretical, computational and experimental tools, how PA signal properties (time and frequency domains) change with cell/tissue pathology and how signal properties can be used for diagnosis. A forward and an inverse problem frameworks have been developed by him in the field of PAs. The forward model has been used to study the effects of RBC aggregation and oxygenation on PA signal, PAs of malaria infected cells, cancer cells with endocytosed gold nanaoparticles and melanoma cells in blood circulation have been examined in detail. An inverse problem framework has been proposed to show how mean size and variance in the absorption coefficient of tissue microstructures can be estimated by performing spectral analysis of PA signals.

Supplementary Materials

Mie

λ pairs	RBC+PLS			RBC+PBS		
	Nominal Hct (%)	**Estimated Hct (%)**	**Estimated SO$_2$ (%)**	**Nominal Hct (%)**	**Estimated Hct (%)**	**Estimated SO$_2$ (%)**
532 nm & 700 nm	50	44.2	11.8	50	43.7	10.8
	45	42.7	13.8	45	42.3	9.0
	40	40.1	15.1	40	40.3	8.8
	30	35.3	24.7	30	35.6	4.5
532 nm & 1000 nm	50	37.5	593.7	50	30.3	2242.4
	45	38.0	551.6	45	33.3	1943.1
	40	38.2	491.5	40	33.8	1800.0
	30	44.5	284.1	30	56.2	800.9
532 nm & 1064 nm	50	34.4	823.7	50	11.4	11507.2
	45	36.9	707.9	45	19.1	6521.1
	40	37.2	635.1	40	28.7	3994.4
	30	48.1	315.6	30	82.6	983.7
700 nm & 1000 nm	50	46.2	47.8	50	45.2	44.4
	45	44.1	48.3	45	43.4	44.7
	40	40.7	47.9	40	41.1	44.4
	30	32.5	47.9	30	33.4	46.2
700 nm & 1064 nm	50	46.6	50.5	50	45.7	48.1
	45	44.2	50.4	45	43.8	48.3
	40	40.9	50.2	40	41.1	47.2
	30	32.1	48.8	30	32.7	47.5
1000 nm & 1064 nm	50	59.4	132.4	50	57.0	140.1
	45	45.9	123.7	45	53.2	139.3
	40	45.3	126.7	40	40.9	132.6
	30	19.0	88.8	30	18.8	104.5

Table S1
The estimated hematocrit and oxygen saturation levels utilizing the simulated PA signals for different pairs of incident optical wavelengths; SO$_2$ = 57% for RBC+PLS samples and SO$_2$ = 65% for RBC+PBS samples; g values provided by the Mie theory have been incorporated in the MC simulations to generate the fluence maps.

Meinke

λ pairs	RBC+PLS			RBC+PBS		
	Nominal Hct (%)	**Estimated Hct (%)**	**Estimated SO_2 (%)**	**Nominal Hct (%)**	**Estimated Hct (%)**	**Estimated SO_2 (%)**
532 nm & 700 nm	50	44.6	36.6	50	44.8	35.3
	45	42.5	39.7	45	42.8	37.8
	40	40.6	45.2	40	40.4	39.6
	30	34.8	53.2	30	34.7	48.2
532 nm & 1000 nm	50	38.0	323.8	50	38.8	467.7
	45	38.0	295.3	45	38.7	435.9
	40	41.2	217.1	40	39.9	366.6
	30	41.7	130.0	30	41.8	237.5
532 nm & 1064 nm	50	37.3	347.0	50	37.0	564.2
	45	37.6	311.7	45	36.9	528.2
	40	40.5	237.3	40	40.9	392.4
	30	43.1	119.2	30	43.4	251.6
700 nm & 1000 nm	50	47.8	57.6	50	46.9	60.6
	45	44.7	58.8	45	44.3	61.5
	40	40.3	59.5	40	40.5	61.0
	30	31.4	60.5	30	32.0	62.7
700 nm & 1064 nm	50	48.0	58.1	50	47.3	62.1
	45	44.8	59.1	45	44.7	63.1
	40	40.6	60.3	40	40.2	61.5
	30	30.8	59.6	30	31.7	63.0
1000 nm & 1064 nm	50	52.5	53.9	50	64.2	114.0
	45	41.9	33.5	45	63.6	116.4
	40	57.8	80.0	40	25.2	48.5
	30	16.1	417.3	30	19.5	45.2

Table S2
Same as Table S1 but g values have been taken from the literature (Meinke dataset: columns 8 and 9 of Table 1).

Donor 1

λ pairs	RBC+PLS			RBC+PBS		
	Nominal Hct (%)	Estimated Hct (%)	Estimated SO_2 ± std (%)	Nominal Hct (%)	Estimated Hct (%)	Estimated SO_2 ± std (%)
532 nm & 700 nm	49	42.9±1.3	81.5±9.5	50	48.9±2.1	72.4±16.2
	45	41.5±1.9	60.5±13.3	45	44.5±2.1	78.1±20.9
	40	39.7±1.5	35.8±15.4	35	37.9±1.9	68.9±13.7
	28	36.6±2.0	13.2±7.6	29	34.6±0.8	44.3±12.6
532 nm & 1000 nm	49	40.6±1.7	303.2±17.3	50	49.0±3.1	551.7±34.1
	45	40.6±2.6	280.2±27.7	45	43.6±3.9	583.1±61.0
	40	39.9±1.7	266.2±17.7	35	38.5±2.6	531.0±44.9
	28	39.1±2.6	207.4±17.3	29	38.3±1.2	421.2±21.8
532 nm & 1064 nm	49	46.4±2.4	547.9±53.7	50	48.6±2.0	651.1±19.1
	45	43.8±1.4	519.8±43.6	45	47.7±2.1	696.2±40.6
	40	40.1±1.5	473.4±28.8	35	33.5±1.1	577.6±31.3
	28	31.2±0.9	318.1±51.1	29	27.3±1.1	480.8±24.3
700 nm & 1000 nm	49	48.5±1.4	54.3±1.9	50	48.8±1.4	70.4±3.3
	45	43.7±1.6	56.8±3.8	45	45.6±2.6	70.4±3.0
	40	39.0±2.4	61.5±3.5	35	37.0±1.7	70.2±3.7
	28	30.5±1.6	61.1±2.6	29	29.5±0.9	70.5±3.3
700 nm & 1064 nm	49	46.4±2.4	5.1±3.9	50	48.6±2.0	23.2±8.7
	45	43.8±1.4	10.9±7.6	45	47.7±2.1	27.5±11.6
	40	40.1±1.5	20.8±11.2	35	33.5±1.1	13.4±10.5
	28	31.2±0.9	19.9±7.4	29	27.3±0.8	15.8±7.7
1000 nm & 1064 nm	49	46.4±2.4	120.9±9.8	50	48.6±2.0	162.6±8.4
	45	43.8±1.4	118.2±9.5	45	47.7±2.1	153.6±12.0
	40	40.1±1.5	122.4±10.8	35	33.5±1.1	180.9±11.7
	28	31.2±0.9	122.2±10.8	29	27.3±0.8	177.6±9.7

Table S3
The estimated hematocrit and oxygen saturation levels for experimental signals (for Donor 1) for different pairs of incident optical wavelengths.

Donor 2

λ pairs	RBC+PLS			RBC+PBS		
	Nominal Hct (%)	**Estimated Hct (%)**	**Estimated SO_2 ± std (%)**	**Nominal Hct (%)**	**Estimated Hct (%)**	**Estimated SO_2 ± std (%)**
532 nm & 700 nm	49	47.8±1.5	75.4±12.7	50	47.9±1.4	122.8±8.2
	45	44.2±1.6	72.4±13.5	46	41.7±1.5	110.0±15.8
	39	40.0±1.8	109.2±15.8	42	41.4±0.9	81.3±9.5
	30	30.4±1.1	60.2±10.1	31	37.6±1.3	38.4±7.8
532 nm & 1000 nm	49	48.4±1.9	268.3±12.2	50	44.3±2.2	506.5±26.9
	45	44.9±2.2	267.6±12.4	46	38.8±2.2	512.8±29.1
	39	38.1±2.7	320.6±27.7	42	42.3±1.5	400.3±13.4
	30	31.3±1.5	270.4±15.1	31	42.6±1.7	293.7±11.3
532 nm & 1064 nm	49	46.6±0.4	831.1±12.8	50	53.1±0.6	742.1±17.5
	45	44.8±0.6	845.3±16.4	46	45.2±0.9	724.5±27.7
	39	43.1±0.7	879.9±18.7	42	40.3±0.5	653.017.3
	30	28.2±0.5	805.4±15.8	31	30.5±0.9	510.2±41.2
700 nm & 1000 nm	49	46.6±1.6	52.5±2.7	50	53.6±0.7	59.1±1.1
	45	42.7±1.7	53.1±2.5	46	46.2±1.5	61.7±2.2
	39	44.2±0.9	50.2±1.9	42	39.9±0.8	61.4±1.5
	30	28.8±0.9	56.0±2.1	31	29.5±0.9	63.3±2.2
700 nm & 1064 nm	49	46.6±0.4	51.7±5.1	50	53.1±0.6	12.3±3.6
	45	44.8±0.6	55.3±4.4	46	45.2±0.9	15.5±8.3
	39	43.1±0.7	47.7±3.7	42	40.3±0.5	18.3±4.7
	30	28.2±0.5	53.9±4.4	31	30.5±0.9	23.8±8.0
1000 nm & 1064 nm	49	46.6±0.4	53.2±0.6	50	53.1±0.6	124.5±1.9
	45	44.8±0.6	50.2±1.0	46	45.2±0.9	131.1±4.7
	39	43.1±0.7	53.0±1.7	42	40.3±0.5	125.7±2.3
	30	28.2±0.5	58.6±1.9	31	30.5±0.9	125.5±5.3

Table S4
Same as Table S3 but for Donor 2.

Donor 3

λ pairs	RBC+PLS			RBC+PBS		
	Nominal Hct (%)	**Estimated Hct (%)**	**Estimated $SO_2 \pm$ std (%)**	**Nominal Hct (%)**	**Estimated Hct (%)**	**Estimated $SO_2 \pm$ std (%)**
532 nm & 700 nm	50	48.4± 2.5	12.5±9.9	48	43.3± 1.7	19.6±4.5
	46	49.8± 1.7	20.6±6.4	44	39.1± 1.5	26.1±6.8
	40	36.5± 1.1	4.9±3.3	38	39.2± 0.9	23.6±6.9
	30	31.2± 1.2	10.4±7.0	30	34.1± 0.8	24.4±9.5
532 nm & 1000 nm	50	47.7± 3.1	143.2±14.6	48	43.6± 2.1	204.2±13.1
	46	51.6± 2.1	109.8±8.1	44	38.6± 2.0	224.8±15.6
	40	35.9± 1.3	163.0±9.4	38	39.3± 1.2	203.6±14.6
	30	30.8± 1.4	140.1±12.3	30	34.1± 1.0	206.0±9.8
532 nm & 1064 nm	50	56.5± 1.0	354.3±51.6	48	42.9± 0.3	453.7±28.1
	46	48.7± 2.3	153.8±74.7	44	41.5± 0.7	508.9±32.5
	40	35.7± 2.6	169.5±70.6	38	38.9± 0.8	456.7±26.3
	30	27.7± 1.2	76.9±55.2	30	33.1± 0.5	439.0±25.6
700 nm & 1000 nm	50	51.2± 1.5	51.7±2.4	48	42.4± 0.6	58.9±1.6
	46	42.3± 1.4	55.8±2.4	44	40.5± 0.8	59.6±1.5
	40	39.1± 0.8	59.6±2.4	38	38.7± 1.2	57.7±2.5
	30	32.5± 1.4	51.8±3.0	30	34.0± 1.4	57.8±2.4
700 nm & 1064 nm	50	56.5± 1.0	25.1±5.5	48	42.9± 0.3	30.1±2.7
	46	48.7± 2.3	34.5±6.1	44	41.5± 0.7	32.2±2.7
	40	35.7± 2.6	19.1±6.9	38	38.9± 0.8	27.7±3.8
	30	27.7± 1.2	7.6±4.6	30	33.1± 0.5	24.8±7.3
1000 nm & 1064 nm	50	56.5± 1.0	81.9±5.7	48	42.9± 0.3	98.9±2.8
	46	48.7± 2.3	83.2±8.7	44	41.5± 0.7	98.6±3.9
	40	35.7± 2.6	118.3±12.2	38	38.9± 0.8	98.2±6.2
	30	27.7± 1.2	113.7±7.8	30	33.1± 0.5	102.2±3.3

Table S5
Same as Table S3 but for Donor 3.